Crustal density and global gravitational field estimation of the Moon from GRAIL and LOLA satellite data

M. Šprlák[a,b,*], S.-C. Han[a], W.E. Featherstone[c]

[a] *School of Engineering, Faculty of Engineering and Built Environment, University of Newcastle, University Drive, Callaghan, NSW 2308, Australia*
[b] *NTIS–New Technologies for the Information Society, Faculty of Applied Sciences, University of West Bohemia, Technická 8, 306 14 Plzeň, Czech Republic*
[c] *School of Earth and Planetary Sciences, Curtin University of Technology, GPO Box U1987, Perth, WA 6845, Australia*

Abstract

We employ Newton's integral in the spectral domain to solve two geodetic/geophysical tasks for the Moon. Firstly, we determine 3D bulk density distribution within the lunar crust (inverse problem). For this purpose, we develop a linear mathematical model that parameterises the laterally variable density component by surface spherical harmonics. We exploit GL1500E GRAIL gravitational field model and LOLA topography model to determine bulk density in three types of function: 1) constant, 2) laterally variable, and 3) 3D spatially variable (assuming a linear change in the radial direction). Secondly, we calculate lunar gravitational field models inferred by these three crustal compositions (forward problem) up to spherical harmonic degree 2519 corresponding to a spatial resolution of ∼2.2 km at the lunar equator. Efficacy of these models is assessed with respect to the GRAIL Level 2 gravitational field models. Our spatially variable crustal model represents the best fit globally and also locally in highland areas. We also test the performance of GRAIL models, recent and independent forward models, and our new models against Level 1B GRAIL satellite-to-satellite tracking data focusing on evaluation beyond Level 2 data (i.e., spherical harmonic degrees greater than 650). These medium- and high-frequency signals from our models correlate with the Level 1B observations the best among all global gravitational field models tested. Our high resolution geopotential model with the optimized 3D crustal density variation should be an asset to future lunar lander navigation and geophysical exploration.

*Tel.:+420 37763 9131, Fax: +420 37763 1112
Email address: michal.sprlak@gmail.com (M. Šprlák)

Keywords: Newton's integral, Forward modelling, LOLA, GRAIL, Bulk density, Crust

Introduction

Lunar gravitational field is useful for understanding the thermal evolution of the Moon (e.g., Laneuville et al., 2013), determining its lunar crustal and lithospheric structure (e.g., Wieczorek et al., 2013; Han, 2013; Andrews–Hanna et al., 2014), constraining the size of the lunar core (e.g., Williams et al., 2014), explaining the origin of mascons (Muller and Sjogren, 1968) and subsurface processes in impact basins (e.g., Melosh et al., 2013; Neumann et al., 2015), improving satellite orbits for topographic mapping by laser altimetry (e.g., Mazarico et al., 2018), and navigating space vehicles (e.g., Miller, 2019).

Numerous gravitational field models have been developed by analysing tracking artificial lunar satellites, such as the Soviet Luna (Akim, 1966), Lunar Orbiter (Muller and Sjogren, 1968), Apollo 15 and 16 subsatellites (Sjogren et al., 1974), Clementine (Zuber et al., 1994), Lunar Prospector (Konopliv et al., 2001), SELenological and ENgineering Explorer (SELENE) (Namiki et al., 2009), and Gravity Recovery And Interior Laboratory (GRAIL) (Zuber et al., 2013). The most recent harmonic expansions from GRAIL significantly outperform the others (e.g., Konopliv et al., 2014; Lemoine et al., 2014) and are available up to degrees 900, 1200, or even 1500. Such spectral and spatial resolutions make the lunar gravitational field the most detailed among all the bodies in the solar system including the Earth.

Alternatively, the lunar gravitational field can be determined by forward modelling that is based on Newton's (1687) integral for the gravitational potential (e.g., Wieczorek and Phillips, 1998; Featherstone et al., 2013; Hirt and Kuhn, 2017; Šprlák et al., 2018). Practically, one exploits any available information about both the bulk density distribution and geometry (specifically topography) of the Moon. Forward models can be attractive, because they can provide high-resolution gravitational field models free from empirical constraints, such as the power law "Kaula's rule" used in the GRAIL-derived global gravitational field models (GGFMs) starting at degree 600 or 700 (Konopliv et al., 2014; Lemoine et al., 2014). In addition, the forward gravitational fields allow different density distributions to be considered, and thus, to test various internal compositions of the Moon.

In this article, we apply our forward method (Šprlák et al., 2018) to determine GGFMs

inferred by different lunar crustal compositions up to degree 2519 (spatial resolution of ∼2.2 km at the lunar equator). Geometrically, the lunar crust is bounded by the high-resolution LOLA topography (Smith et al., 2010) and a crust-mantle interface (Wieczorek et al., 2013). Several regional (Liang et al., 2014; Jansen et al., 2017; Zhang et al., 2018; Zhao et al., 2019; Zhong et al., 2019) or global (Wieczorek et al., 2013; Han, 2013; Besserer et al., 2014; Wahl and Oberst, 2019) density maps have already been provided from LOLA and GRAIL. Here, we calculate independent bulk density for the lunar crust in three types of function: 1) a constant, 2) laterally variable, and 3) 3D spatially variable (assuming a linear change in the radial direction). For this purpose, we develop a global and fully spherical mathematical model that allows determining the density from the knowledge of the outer gravitational field, i.e., geophysical inversion. We parametrise the laterally variable density by surface spherical harmonics, i.e., in the spectral domain by spherical harmonic coefficients. This is different from the previous studies estimating density values directly in the spatial domain. Performance of the gravitational fields inferred by these three crustal density models is tested with respect to a GRAIL-derived model and Level 1B range acceleration data.

1. Methods and data

1.1. Forward gravitational field modelling

Forward modelling may be employed in the spatial domain when the gravitational potential and its functionals are calculated by discretising Newton's integral and its higher-order spatial derivatives. Alternatively, we may evaluate a spectrum of the gravitational potential. The spectrum defines any gravitational field quantity that may be synthesised in the corresponding convergence domain (i.e., outside the gravitating masses or so-called Brillouin sphere) by a harmonic series. We prefer the spectral representation due to its practical advantages, as described later.

The 4π fully normalised gravitational potential spherical harmonic (Stokes's) coefficient $\bar{C}_{n,m}$ of degree n and order m is given by (e.g., Heiskanen and Moritz, 1967, Sect. 2.5):

$$\bar{C}_{n,m} = \frac{1}{R^n M(2n+1)} \int_{\lambda=0}^{2\pi} \int_{\varphi=-\pi/2}^{\pi/2} \bar{Y}_{n,m}(\varphi,\lambda) \int_{r=r_1(\varphi,\lambda)}^{r_2(\varphi,\lambda)} \rho(r,\varphi,\lambda)\, r^{n+2}\, \mathrm{d}r\, \cos\varphi\, \mathrm{d}\varphi\, \mathrm{d}\lambda\,. \tag{1}$$

The symbol R stands for the radius of the Brillouin sphere, M is the total mass of the gravitating body, and the triplet of the spherical coordinates is defined by the spherical radius r, spherical latitude φ, and spherical longitude λ. The crustal masses of the bulk density ρ are limited by the crust-mantle interface (indicated by the spherical radius r_1) and the lunar topography (specified by the spherical radius r_2). The scalar 4π normalised spherical harmonics $\bar{Y}_{n,m}$ are (Abramowitz and Stegun, 1972, Sect. 8):

$$\bar{Y}_{n,m}(\varphi,\lambda) = \bar{P}_{n,|m|}(\sin\varphi) \begin{cases} \cos m\lambda\,, \forall m \geq 0 \\ \sin|m|\lambda\,, \forall m < 0 \end{cases}, \tag{2}$$

where $\bar{P}_{n,|m|}$ are the 4π fully normalised associated Legendre functions of the first kind.

All gravitational field models in this article refer to the Brillouin sphere of radius $R = 1748.2$ km. We determined R by finding the maximum of the selenocentric spherical radius r_2 from LOLA, and rounding this value up to the nearest 50 metres. We follow the notion of the Brillouin sphere encompassing all gravitating masses, because it guarantees the harmonicity of the external gravitational field and the convergence of the related spherical harmonic series (e.g., Moritz, 1989, Chap. 6 and 7).

For practical calculations, Eq. (1) has to be discretised. Within this article, we calculate gravitational potential spectra by the rigorous forward modelling approach, which was developed and extensively tested by Šprlák et al. (2018).

1.2. Mathematical model for crustal density estimation

The starting point of our bulk density estimation method is a functional relationship for ρ. We decompose the bulk density into a surface component and a radial part, i.e.:

$$\rho(r,\varphi,\lambda) = \rho(\varphi,\lambda) + \alpha\big[r_2(\varphi,\lambda) - r\big] = \sum_{n,m}^{N_{max}} \bar{\rho}_{n,m}\,\bar{Y}_{n,m}(\varphi,\lambda) + \alpha\big[r_2(\varphi,\lambda) - r\big]\,. \tag{3}$$

The sign $\sum_{n,m}^{N_{max}}$ substitutes for the double summation $\sum_{n=0}^{N_{max}}\sum_{m=-n}^{+n}$. We have expanded the surface part by the (surface) spherical harmonic series up to the maximum degree N_{max} with

the harmonic coefficients:

$$\bar{\rho}_{n,m} = \frac{1}{4\pi} \int_{\lambda=0}^{2\pi} \int_{\varphi=-\pi/2}^{\pi/2} \rho\big(\varphi,\lambda\big)\, \bar{Y}_{n,m}\big(\varphi,\lambda\big)\, \cos\varphi \,\mathrm{d}\varphi \,\mathrm{d}\lambda \,. \tag{4}$$

The symbol α in Eq. (3) is the (assumed linear) radial density gradient.

We now substitute for the density ρ in Eq. (1) by the right-hand side of Eq. (3). Because we have enforced uniform convergence of the spherical harmonic expansion by using the Brillouin sphere, we may change the order of summation and integration. By exploiting the rules of integral calculus, we express two integrals over the variable r analytically in the form:

$$E_n\big(R,\varphi,\lambda\big) = \frac{1}{R^n} \int_{r=r_1(\varphi,\lambda)}^{r_2(\varphi,\lambda)} r^{n+2}\,\mathrm{d}r = \frac{R^3}{n+3} \left\{ \left[\frac{r_2\big(\varphi,\lambda\big)}{R}\right]^{n+3} - \left[\frac{r_1\big(\varphi,\lambda\big)}{R}\right]^{n+3} \right\}, \tag{5}$$

$$F_n\big(R,\varphi,\lambda\big) = \frac{1}{R^n} \int_{r=r_1(\varphi,\lambda)}^{r_2(\varphi,\lambda)} \big[r_2\big(\varphi,\lambda\big) - r\big]\, r^{n+2}\,\mathrm{d}r = R^4 \left\{ \frac{1}{(n+3)(n+4)} \left[\frac{r_2\big(\varphi,\lambda\big)}{R}\right]^{n+4} \right.$$

$$\left. + \left[\frac{1}{n+4} - \frac{r_2\big(\varphi,\lambda\big)}{r_1\big(\varphi,\lambda\big)(n+3)}\right] \left[\frac{r_1\big(\varphi,\lambda\big)}{R}\right]^{n+4} \right\}. \tag{6}$$

These mathematical operations and substitutions lead to:

$$\bar{C}_{n,m} = \frac{1}{M(2n+1)} \left[\sum_{n',m'}^{N_{max}} \bar{\rho}_{n',m'} \int_{\lambda=0}^{2\pi} \int_{\varphi=-\pi/2}^{\pi/2} \bar{Y}_{n,m}\big(\varphi,\lambda\big)\, \bar{Y}_{n',m'}\big(\varphi,\lambda\big)\, E_n\big(R,\varphi,\lambda\big)\, \cos\varphi \,\mathrm{d}\varphi \,\mathrm{d}\lambda \right.$$

$$\left. + \alpha \int_{\lambda=0}^{2\pi} \int_{\varphi=-\pi/2}^{\pi/2} \bar{Y}_{n,m}\big(\varphi,\lambda\big)\, F_n\big(R,\varphi,\lambda\big)\, \cos\varphi \,\mathrm{d}\varphi \,\mathrm{d}\lambda \right]. \tag{7}$$

The last expression is the standard Gauss-Markov linear model (e.g., Grafarend, 2006, Sect. 2.1):

$$\mathbf{l} = \mathbf{A}\,\mathbf{x} + \boldsymbol{\epsilon}\,. \tag{8}$$

The observation vector $\mathbf{l}$ contains the spherical harmonic coefficients $\bar{C}_{n,m}$ of the gravitational potential. These are available from the lunar GGFMs that serve as "observables" in our experiments. The two integrals over the spherical coordinates φ and λ in Eq. (7) form the elements of the design matrix $\mathbf{A}$. These integrals are discretised and calculated numerically from available grids of the lunar topography and the crust-mantle interface, see below. The vector $\mathbf{x}$ is composed of the spherical harmonic coefficients $\bar{\rho}_{n',m'}$ of the surface density and the linear density gradient α. The symbol $\boldsymbol{\epsilon}$ is the error vector and we assume that the errors are Gaussian with zero mean.

The linear model of Eq. (8) envelopes three distinct bulk densities that we consider in our experiments, see Sects. 2 and 3:

1) constant, when $\mathbf{x} = \left[\bar{\rho}_{0,0}\right]$,
2) laterally variable, when $\mathbf{x} = \left[\bar{\rho}_{n',m'}\right]$, $n', m' = 0, 1, \ldots, N_{max}$,
3) 3D spatially variable, when $\mathbf{x} = \left[\bar{\rho}_{n',m'} \quad \alpha\right]$, $n', m' = 0, 1, \ldots, N_{max}$.

The density in Eq. (3) can be approximated by more complex functions of the radius r, such as higher-order polynomials or an exponential function (e.g., Ramillien, 2002; Novák and Grafarend, 2006; Besserer et al., 2014; Han et al., 2014). We derived and numerically tested a quadratic vertical density gradient, but could not get any reasonable estimates. Also, we considered application of an exponential density gradient. However, integrals of the exponential function multiplied by the power functions of r (see the integrals of Eqs. (5) and (6)) cannot be solved analytically. To overcome this, the exponential function is sometimes expressed by a power series that results in a polynomial density expansion (Eshagh, 2009). As such, this method suffers the same setbacks as the quadratic gradient.

1.3. LOLA lunar topography

We used the lunar topography provided by the Lunar Orbiter Laser Altimeter (LOLA) (Smith et al., 2010). Namely, we exploited the global and regularly sampled LOLA heights with the discretisation of 1/64°, see `http://pds-geosciences.wustl.edu/lro/lro-l-lola-3-rdr-v1/lrolol_1xxx/data/lola_gdr/cylindrical/pa/`. The LOLA heights are referenced to the sphere of radius 1737.4 km in the principal axis coordinate system, which is consistent with that of GRAIL GGFMs.

Initially, we calculated a smoother LOLA topography with sampling of 1/14° by the routine *blockmean* from the Generic Mapping Tools (Wessel et al., 2013). The 1/14° grid was utilised in the computation of the crustal densities and the crustal GGFMs up to the corresponding spherical harmonic degree of 2519. However, our gravitational field models were visibly smoother at high frequencies than GRAIL Level 1B observations, see Sect. 3.2. To describe the lunar gravitational field most realistically, we finally used a more detailed LOLA grid with sampling of 1/56° for both, density estimation and forward modelling, but our crustal GGFMs were still calculated up to degree 2519.

1.4. GRAIL gravitational fields

We employed spherical harmonic parameterisations of the lunar gravitational field produced by the NASA GRAIL team. Namely, we adopted GL1500E (Konopliv et al., 2014) for the density estimation in Sect. 2 and for validation of our forward models in Sects. 3.1 and 3.2. GRGM0900C and GRGM1200A (Lemoine et al., 2014) were included in the model comparison in Sect. 3.2.

These three GRAIL models represent contemporary solutions (at the time of writing) determined from the entire GRAIL mission. Their spherical harmonic coefficients refer to the sphere of radius 1738 km, so were continued to the Brillouin sphere of radius $R = 1748.2$ km for consistency with our forward modelling. These three gravitational field models are distinct in the maximum spherical harmonic degree (indicated by their name), data pre-processing, data weighting, power law constraint at high-frequencies, etc.

1.5. Other forward global gravitational field models

For the numerical investigations in Sect. 3.2, we also considered two independently computed forward-modelled GGFMs by Hirt and Kuhn (2017) and Bucha et al. (2019) (herein abbreviated by HK2160 and STU2160 to also indicate their maximum degrees). Both models use the finite-amplitude method (Wieczorek and Phillips, 1998) and assume a constant density of 2500 kg m^{-3} for the topographic (crustal) masses.

These two forward models differ by their geometry of the crustal masses. HK2160 is generated by the masses between the sphere of radius 1738 km and the lunar shape model expanded up to degree 2160 (Hirt and Kuhn, 2017). STU2160 used the same sphere, but the shape model was

coarser and expanded only up to degree 720 (Bucha et al., 2019). We also note that STU2160 is a forward-modelled gravitational field determined by iterative downward continuation to a Bjerhammar sphere of radius 1737.999 km.

1.6. Lunar crust-mantle boundary

We used an irregular (i.e., non-spherical) crust-mantle boundary $r_1 = r_1(\varphi, \lambda)$ from the GRAIL Crustal Thickness Archive (Wieczorek et al., 2013). We adopted the crustal thickness model no. 3, which was estimated by GL0420A truncated beyond degree 310, with a crustal porosity of 12%, mantle density of 3150 kg m^{-3}, and a downward continuation filter of 0.5 at degree 70. The crustal thickness model is available in terms of spherical harmonic coefficients up to degree 310. We synthesised the corresponding crust-mantle boundary with equiangular sampling of $1/56^\circ$ so as to be consistent with the LOLA topography grid used in our computations.

2. Estimates of the lunar crustal density

2.1. Constant density

We begin our numerical experiments with the simplest approximation of a constant crustal density. This is simplistic, but allows initial validation of the numerical set-up and restricting the input parameters for further experiments with more complex density distributions.

We found least-squares estimates of the constant density by solving the overdetermined equation system:

$$\hat{\mathbf{x}} = \left(\mathbf{A}^{\mathrm{T}}\,\mathbf{A}\right)^{-1}\,\mathbf{A}^{\mathrm{T}}\,\mathbf{l}\,. \tag{9}$$

The observation vector $\mathbf{l}$ was composed of the coefficients $\bar{C}_{n,m}$ between degrees 150-600 (in total 338,701 entries). We chose this spectral band because the observed lunar gravitational field and the one inferred by topography are highly correlated above degree 150 (e.g., Konopliv et al., 2014; Lemoine et al., 2014), see also Fig. 3 herein. The elements of the design matrix $\mathbf{A}$ were calculated by discretising the first integral in Eq. (7). Because the constant density is the only unknown, the design matrix $\mathbf{A}$ degenerates into a column vector of the same size as the

observation vector $\mathbf{l}$. We obtained the density of 2540.6 $\pm$ 0.6 kg m^{-3}. This estimate agrees very well with 2544 kg m^{-3} by Han (2013) or 2550 kg m^{-3} by Wieczorek et al. (2013).

Numerous calculations (parameter sweeps) were performed to test how various parameters and models (crust-mantle boundary, gravitational, and topography) contribute to the constant density estimation. In particular, we found that:

- Density was significantly overestimated by smoothing the lunar topography. For example, we obtained density estimates of $\sim$2700 kg m^{-3} when taking the LOLA grid with sampling of 3/10° (corresponding to spherical harmonic degree 600).

- We obtained underestimated values by increasing the lower limit of the harmonic band (e.g., Han, 2013). For example, we obtained densities of $\sim$2500 kg m^{-3} when considering the coefficients $\bar{C}_{n,m}$ between degrees 300-600. This is because higher degrees are more sensitive to the upper parts of the lunar crust with higher porosity, and thus lower density.

- One may expect slightly higher values of density by decreasing the upper limit of the harmonic band. For example, density increased by 2-3 kg m^{-3} by considering $\bar{C}_{n,m}$ between degrees 150-300. Lower harmonic degrees are more sensitive to the lower parts of the lunar crust with lower porosity. This also explains why the values by Han (2013) and Wieczorek et al. (2013), who employed the spectral bands 150-300 and 150-310, respectively, are larger by $\sim$3 and $\sim$9 kg m^{-3} with respect to our estimate of 2540.6 $\pm$ 0.6 kg m^{-3}.

- The most recent geometries of the crust-mantle boundary may affect the density by 1-2 kg m^{-3}. We proved this assertion by considering all four crustal thickness models from the GRAIL Crustal Thickness Archive in our calculations.

- The gravitational effect of mantle masses influences density estimate by $\sim$5 kg m^{-3}. This was found for constant mantle density of 3150 kg m^{-3}. We chose the base of the mantle at a radius of 380 km (Garcia et al., 2011), while the upper boundary of the mantle was represented by the crust-mantle boundary described in Sect. 1.6.

- Density estimates from up-to-date and highest-resolution GRAIL-derived GGFMs were almost identical. For example, we used $\bar{C}_{n,m}$ from GRGM1200A (Lemoine et al., 2014)

between degrees 150-600 and found that the density was different to that from GL1500E by 0.001 kg m^{-3}.

- These numerical experiments indicate that our mathematical model is most sensitive to the spatial resolution of topography and to the spectral resolution of the GGFM. Other parameters or alterations of models contribute few to several kg m^{-3} that is currently negligible in constraining the lunar crustal density.

In the following, we keep our initial choice of the input parameters and models, i.e., we use GL1500E between degrees 150-600, LOLA, and GL0420A crust-mantle boundary with equiangular sampling 1/56°, and neglect the gravitational effect of the mantle.

2.2. Laterally variable density

We now consider a spatially variable density distribution that is a function of φ and λ. We determined $\bar{\rho}_{n',m'}$, see Eq. (7), up to $N_{max} = 90$ (spatial resolution of ∼61 km at the Brillouin sphere) that reveals the finest structures of the lunar surface density as compared to the global maps by (Wieczorek et al., 2013; Han, 2013; Besserer et al., 2014). The corresponding system of linear equations was represented by 338,701 observables and 16,562 unknowns and is still solvable by available computer resources.

We also tested higher-degree density expansions, for example, up to $N_{max} = 180$ or 360. However, as shown in Fig. 1, the power of the density signal for $n > 90$ is merely a few kg m^{-3} that is currently negligible in constraining the lunar crustal density based on GRAIL and LOLA data.

The condition number of the normal matrix was $\sim 10^5$. Its magnitude was relatively low compared to the threshold of $\sim 10^{15}$ for the loss of all significant digits in double precision arithmetic. The normal matrix could be still inverted and the least-squares solution of Eq. (9) may eventually provide feasible results.

In contrast to our expectation, the signal power determined by least squares (black line in Fig. 1) does not decrease monotonically with increasing harmonic degree for $n > 4$. Figure 2a illustrates the corresponding spatial map of the laterally variable density. It can be seen that high-frequency noise dominates over low-frequency density features. Thus, the least-squares

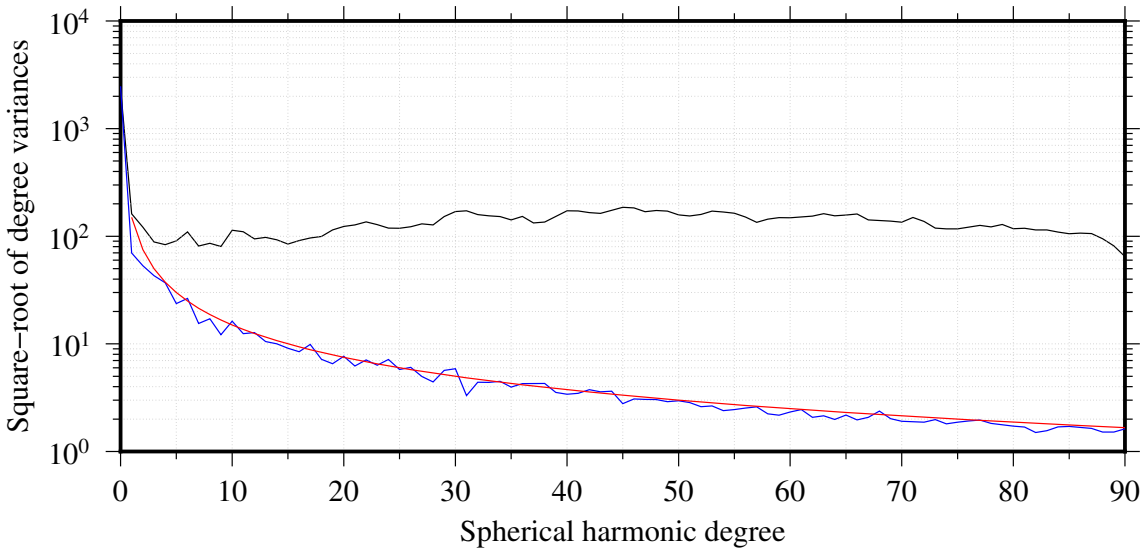

Figure 1: Square root of degree variances from $\bar{\rho}_{n',m'}$. The density coefficients were estimated by least-squares (black) and its regularised counterpart (blue) with the power law constraint $150/n$ (red).

solution of Eq. (9) does not provide any reasonable estimate of laterally variable lunar crustal density.

To spatially constrain the laterally variable density, we added a regularisation matrix $\mathbf{K}$ to the normal matrix and found solutions by (e.g., Bouman, 1998, p. 32):

$$\hat{\mathbf{x}} = \left(\mathbf{A}^{\mathrm{T}}\,\mathbf{A} + \mathbf{K}\right)^{-1}\,\mathbf{A}^{\mathrm{T}}\,\mathbf{l}. \tag{10}$$

We used diagonal $\mathbf{K}$, whose non-zero elements were chosen such that the square root of degree variance for $\bar{\rho}_{n',m'}$ followed the power law $150/n$; see the blue and red lines in Fig. 1. This power law was empirically found from the density maps in Han (2013, Fig. 14a).

The coefficients $\bar{\rho}_{n',m'}$ estimated by Eq. (10) resulted in the density map depicted in Fig. 2b. The high-frequency noise was suppressed. The prominent features are seen with lateral density varying by several 100 kg m^{-3}. The density is the lowest ($\sim$2200 kg m^{-3}) in the Procellarum KREEP Terrane and reaches the largest values (2700-2800 kg m^{-3}) in the South-Pole Aitken basin.

We compared our regularised solution with the one by Wieczorek et al. (2013), see Fig. 2c. Blank regions can be identified in Fig. 2c over the lunar maria and low-elevation areas resurfaced by basaltic lava flows. Here, the correlation between the observed and topography-inferred

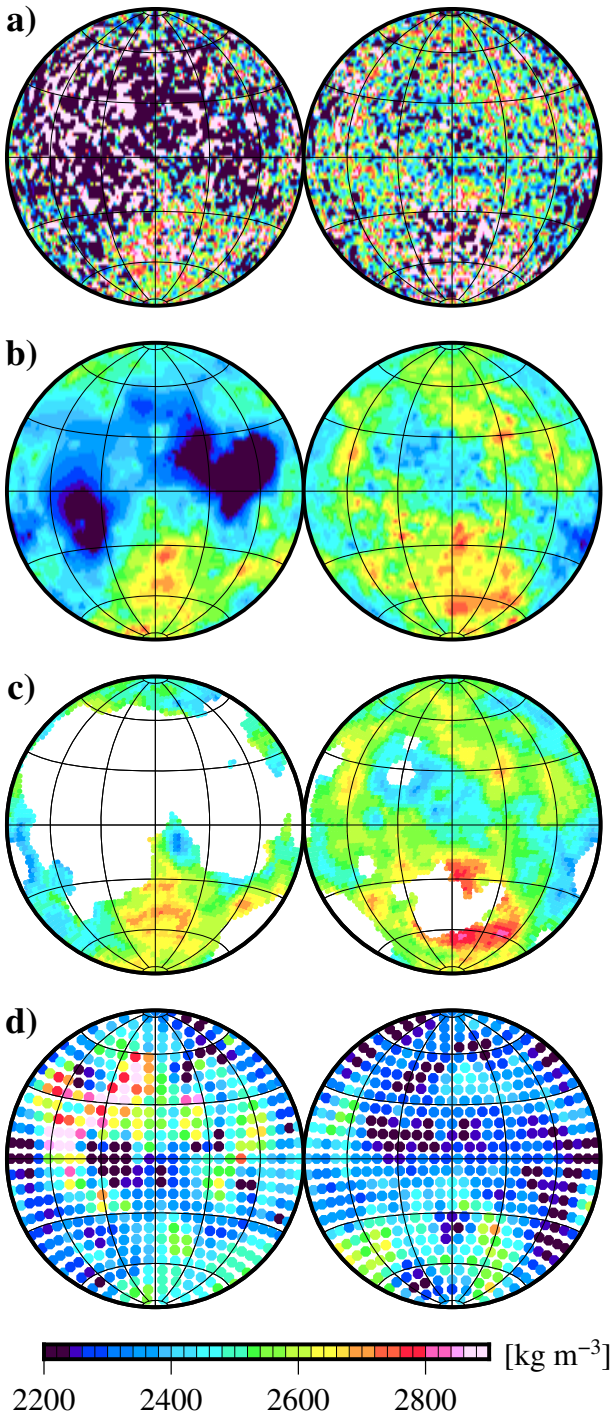

Figure 2: The laterally variable density maps determined by: **a)** least-squares of Eq. (9), **b)** regularised least-squares of Eq. (10), **c)** Wieczorek et al. (2013), and **d)** Besserer et al. (2014). The densities in maps **a)** and **b)** were synthesised up to $N_{max} = 90$ at equiangular spacing of 2°. The maps were generated in an orthographic projection centred at $\varphi = \lambda = 0°$ (left hemispheres), and at $\varphi = 0°$, $\lambda = 180°$ (right hemispheres). Left hemispheres depict the nearside and right hemispheres depict the farside. Parallels and meridians are spaced at 30° intervals.

gravitational field is reduced and estimated values may not be reliable. This also holds for the estimates in the blank regions obtained by our method. For a consistent comparison, we synthesised densities from $\bar{\rho}_{n',m'}$ at the same grid points as in Fig. 2c. We truncated the series in Eq. (3) at degree 15. This harmonic degree approximately corresponds to the angular diameter of 12° used for the spherical cap analysis conducted by Wieczorek et al. (2013).

We found that our solution agreed with the one reported by Wieczorek et al. (2013). This is supported by a high correlation coefficient of 0.90 and a standard deviation of differences of ± 35 kg m^{-3}. Our densities were slightly smoother at $N_{max} = 15$, because the result of the approach by Wieczorek et al. (2013) in the spectral domain does not exactly match with the sharp spectral localisation at N_{max} =15 used in our analysis. We emphasise, however, that our solution is not restricted to degree 15. Our density map shows much finer details at $N_{max} = 90$ than the one by Wieczorek et al. (2013); see Figs. 2b and 2c.

The results of this Section indicate that our density estimates appear realistic and comparable with those computed by other authors. Our solution in the form of $\bar{\rho}_{n',m'}$ allows for synthesising laterally variable density at arbitrary locations and with varying spectral (and spatial) resolutions that may be advantageous to previous estimates by (e.g., Wieczorek et al., 2013; Han, 2013; Besserer et al., 2014; Wahl and Oberst, 2019) performed purely in the spatial domain.

2.3. 3D spatially variable density

The density of the lunar crust increases with depth as porosity decreases (e.g., Wieczorek et al., 2013; Han et al., 2014). Therefore, we extended our laterally variable density by a (global) linear density gradient. The design matrix $\mathbf{A}$ was augmented by one column, see the second integral over the angular spherical coordinates in Eq. (7), and the vector $\mathbf{x}$ contained one more unknown parameter α.

We again added the regularisation matrix $\mathbf{K}$ to the normal matrix, because the least-squares solution of Eq. (9) provided an impractical solution. The elements of $\mathbf{K}$ for $\bar{\rho}_{n',m'}$ were identical to those in Sect. 2.2. The element of $\mathbf{K}$ corresponding to α was set to the highest value that still preserved the $\bar{\rho}_{0,0}$ coefficient from the estimate of the laterally variable density determined in Sect. 2.2.

The regularised solution of Eq. (10) slightly changed the estimated laterally variable surface

density by a few kg m^{-3}. More importantly, we found the linear gradient $\alpha = 10.2 \pm 1.5$ kg m^{-3} km^{-1}. We emphasise that this global value is reliable in the areas where the observed and topography-inferred gravitational field correlate the most, see Fig. 2c.

Besserer et al. (2014) considered even more complicated composition of the lunar crust. They decomposed the density into the surface part and a radial part; see the expression after the first equality in Eq. (3). Their radial part, represented by either a linear or an exponential gradient, was also laterally variable. They used a planar approximation of the Moon and performed localised multi-taper analysis with the spherical harmonic coefficients of GRGM900B (Lemoine et al., 2014) between degrees 250-550.

Accordingly, we also incorporated the density decomposed into a laterally variable surface part and laterally variable linear gradient. For this, we expanded the linear gradient into the series of surface spherical harmonics $\sum_{n,m}^{N_{max}} \bar{\alpha}_{n,m} \bar{Y}_{n,m}(\varphi, \lambda)$, see Eq. (3). The mathematical model was similar to Eq. (7), however, we changed $\alpha \rightarrow \sum_{n'',m''}^{N_{max}} \bar{\alpha}_{n'',m''}$ and the second integral over the angular spherical coordinates included spherical harmonics $\bar{Y}_{n'',m''}(\varphi, \lambda)$ that augmented the design matrix $\mathbf{A}$. The vector $\mathbf{x}$ of the corresponding linear model, see Eq. (8), was composed of the density coefficients and the linear gradient coefficients, i.e., $\mathbf{x} = \begin{bmatrix} \bar{\rho}_{n',m'} & \bar{\alpha}_{n'',m''} \end{bmatrix}$, $n', m' = 0, 1, \ldots, N_{max}$; $n'', m'' = 0, 1, \ldots, N_{max}$.

We used this adapted linear model to estimate coefficients $\bar{\rho}_{n',m'}$ and $\bar{\alpha}_{n'',m''}$ up to $N_{max} = 6$. This degree approximately corresponds with the angular size of the spherical caps (diameter of 30°) used in the analysis by Besserer et al. (2014). The observation vector $\mathbf{l}$ was formed by $\bar{C}_{n,m}$ between degrees 250-550. The application of least-squares was not feasible and its regularised version was used instead. The diagonal elements of the $\mathbf{K}$ matrix were selected such that the square root of degree variance from $\bar{\rho}_{n',m'}$ was proportional to n^{-1} and that from $\bar{\alpha}_{n'',m''}$ was proportional to $\sqrt{n}$. These power laws were found by spherical harmonic analysis of the spatial maps of Fig. 1 in (Besserer et al., 2014).

We synthesised density values at the identical grid points as in Besserer et al. (2014) and found that their spatial patterns were different from others; see Fig. 2d. In particular, our densities were larger on the farside of the Moon. In this region, the correlation coefficient between the two solutions was only 0.52, the standard deviation of differences reached ±88 kg m^{-3}, and the mean of differences was 132 kg m^{-3}. We also observed that the values of the linear

gradient from our solution were smaller by approximately one order of magnitude. Reasons for inconsistent results for 3D density structure (i.e., laterally variable density and laterally variable linear gradient) between Besserer et al. (2014) and ours are uncertain.

3. High-resolution crustal gravitational field models from variable densities and their assessment

The three crustal density distributions generate distinct gravitational fields. In this Section, we assess the efficacy of these three models with respect to a GRAIL-derived GGFM between degrees 150-600. In addition, we compare GRAIL Level 2 GGFMs, the HK2160 and STU2160 forward models, and our crustal-density-inferred GGFMs with Level 1B (L1B) GRAIL data to test their performance at high-degrees ($n > 650$).

3.1. Comparison with GRAIL Level 2 geopotential model GL1500E

We firstly assessed our crustal gravitational potential spectra in terms of the global correlation, admittance, and the Bouguer correlation; see Fig. 3. In general, these spectral characteristics are significantly reduced for degrees below 150. Geophysical processes that are not associated with the topographic features, e.g., due to mantle heterogeneities and mare basalts, are dominant at low spherical harmonic degrees and our model does not consider these. Also, the three spectral characteristics gradually decrease above degree 600, because GL1500E is affected by the GRAIL observation noise and the constant power law constraint.

The correlation spectrum between GL1500E and the gravitational field of the uniform crust is depicted in Fig. 3a. The correlation spectra for the other density distributions are indistinguishable from this. The highest correlation values (close to unity) can be seen between degrees 150-600. This spectral range is in agreement with the one selected for the density estimation in Sect. 2.

The admittance spectra are illustrated in Fig. 3b. The admittances (near-linearly) decrease between degrees 150 and 600; those for the constant and laterally variable crustal density models (black and blue curves) with nearly the same gradient (1.0 at degree 150 and 0.93 at degree 700). Among the three density distributions, the 3D spatially variable (red curve) provides the admittance spectrum with the lowest slope and is the closest to unity, indicating the vertical

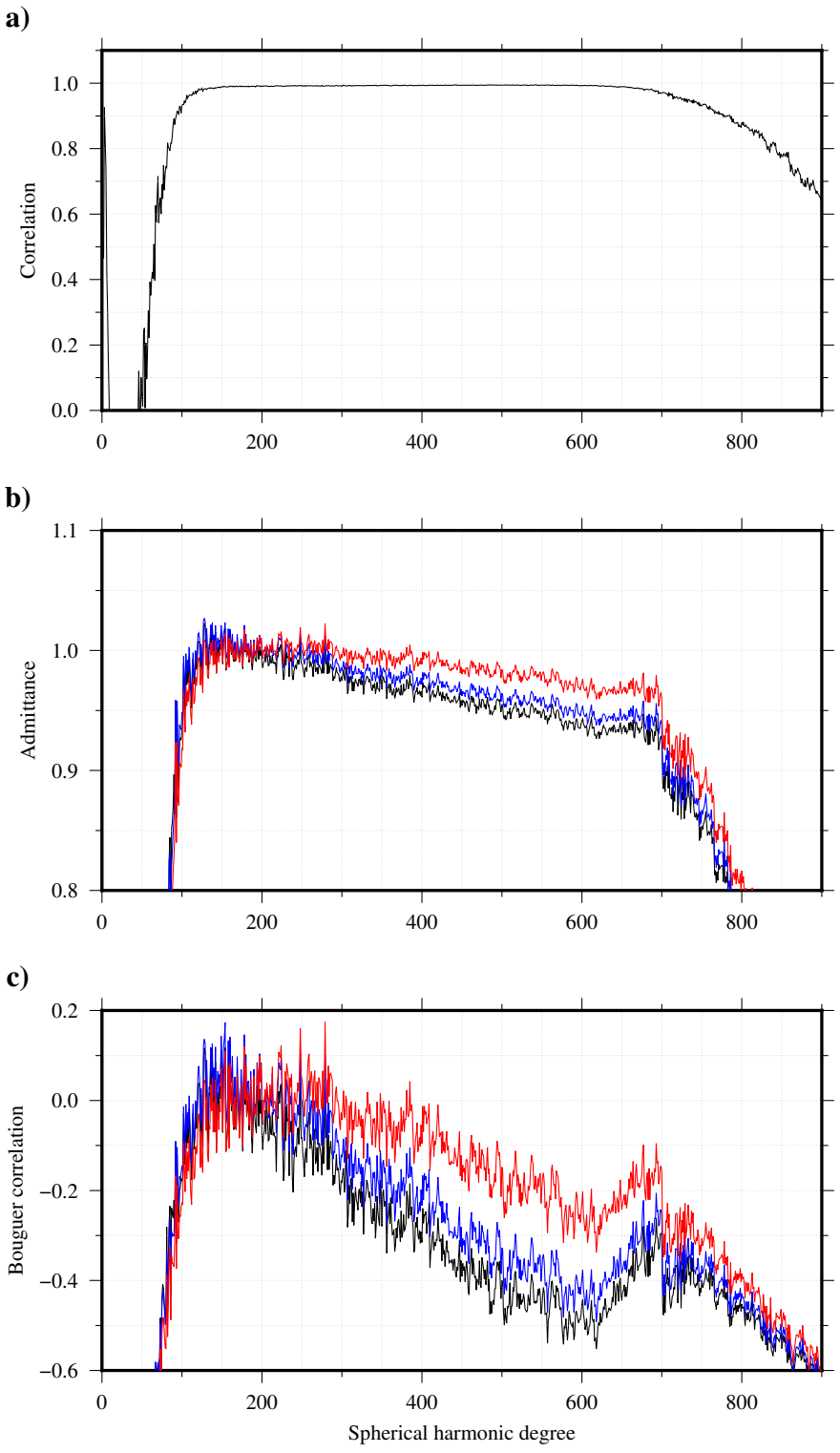

Figure 3: Spectral measures of **a)** correlation, **b)** admittance, and **c)** Bouguer correlation between the GRAIL-only GL1500E and our three forward GGFMs from our different density models: constant (black), laterally variable (blue), and 3D spatially variable (red).

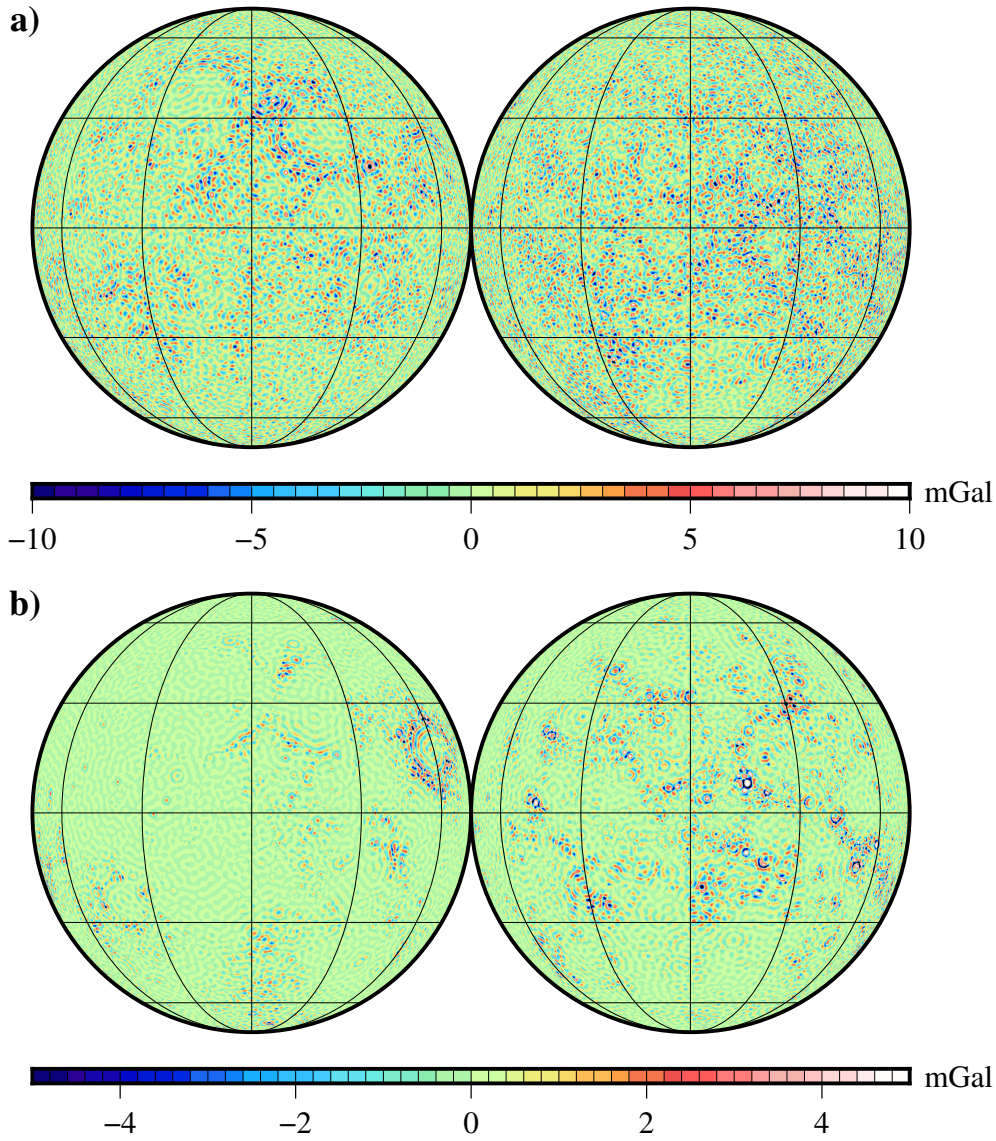

Figure 4: Global maps of: **a)** the Bouguer radial gravitation, and **b)** the differences between the Bouguer radial gravitations inferred by the 3D spatially variable and constant density crusts. The maps are generated in orthographic projection centred at $\varphi = \lambda = 0^\circ$ (left hemispheres), and at $\varphi = 0^\circ$, $\lambda = 180^\circ$ (right hemispheres). Left hemispheres depict the nearside and right hemispheres depict the farside. Parallels and meridians are spaced at 30° intervals.

bulk density decrease (porosity increase) toward surface is favourably represented by our 3D density distribution. The Bouguer correlation spectra behave similarly, i.e., they drop linearly between degrees 150-600; see Fig. 3c, and the Bouguer anomalies from our 3D spatially variable density are de-correlated better than those from the constant and laterally variable densities.

To exemplify the three density distributions in the spatial domain, we calculated the Bouguer radial gravitation, i.e., the negative Bouguer gravity disturbance. This quantity was synthesised

between degrees 150-600 on the Brillouin sphere with the equiangular step of 3/10°.

Figure 4a shows the Bouguer radial gravitation from our geopotential model with the 3D density that reaches a magnitude of 19 mGal and standard deviation of 2 mGal, see Table 1. We can identify larger variations in the farside due to more rugged topography. On the other hand, the Bouguer field is smoother over the nearside, especially over the flat low-elevated mare areas. Compared to the constant density crustal model, the global extrema are reduced by several mGal and the variations are lower by several percent. The radial gravitations generated by the more complex density distributions indeed explain better the observed counterpart than those from the constant density distribution.

Density	Min.	Max.	Mean	Std. dev.
C	-19.51	18.69	0.01	2.19
L	-18.91	15.06	0.01	2.03
S	-18.99	14.10	0.01	2.03
L minus C	-8.57	11.73	0.00	0.59
S minus C	-9.04	11.43	0.00	0.60
L minus S	-1.76	1.41	0.00	0.11

Table 1: Global statistics (in mGal) of the Bouguer radial gravitation from the constant (C), laterally variable (L), and 3D spatially variable (S) density crusts and of their differences.

Area	Density	Min.	Max.	Mean	Std. dev.
Nearside	C	-7.18	7.64	0.01	1.92
	L	-7.51	7.26	0.01	1.75
	S	-7.54	7.31	0.01	1.75
Farside	C	-16.97	16.33	0.00	3.39
	L	-15.54	14.22	0.00	2.99
	S	-14.62	14.14	0.00	2.98
Crisium	C	-14.61	13.61	0.00	2.91
	L	-11.49	12.76	-0.01	2.42
	S	-11.64	12.80	-0.01	2.43

Table 2: Statistics (in mGal) of the Bouguer radial gravitations from the constant (C), laterally variable (L), and spatially variable (S) density of crust.

The differences between the Bouguer radial gravitations from the 3D spatially variable and constant density crustal models are depicted in Fig. 4b. The largest deviations of greater than

10 mGal in magnitude occur on the farside, but differences of several mGal can also be found on the nearside. A similar spatial pattern can be observed when comparing the lateral density gravitational field with its constant-density counterpart. The gravitational fields from the laterally and 3D spatially variable densities are very close and differ by less than 1.8 mGal in magnitude globally, see Table 1.

Regional maps of the Bouguer gravitational fields are presented in Fig. 5 and the corresponding statistics are summarised in Table 2. We selected two highland areas, one in the nearside and another on the farside, where we expect the estimates of the laterally and 3D spatially variable densities to be most reliable. Thus, the corresponding gravitational fields are supposed to exhibit a better fit to GL1500E than that from the constant density. In addition, we chose Mare Crisium because the Bouguer radial gravitations between the 3D spatially variable and constant density crusts differ the most here among all mare regions; see Fig. 4b. We eventually illustrate that the more complex density distributions provide realistic gravitational fields in this mare area.

The local extrema are reduced for the 3D spatially variable density (right) as compared to the constant one (left). The variations of Bouguer gravitational field are reduced by 9% in the nearside highlands, 12% in the farside highlands, and 17% in Mare Crisium, see Table 2. Equivalent to the global investigations, the laterally variable density GGFM is almost identical with the one inferred by the 3D spatially variable density crust for the spectral range 150-600.

To better understand the performance of the three density distributions in these areas, we also calculated (spherical cap) localised spectra (cf., Wieczorek and Simons, 2005). The spherical cap windows of 20° radius were centred in the middle of the three regions and expanded in the spherical harmonic bandwidth 0-20. Other cap sizes and maximum harmonic degrees of the bandwidth were tested, but did not show any sensible difference.

Figure 6 presents the correlations (left) and admittances (right) in the three regions. The Bouguer correlations are omitted from presentation here, because they quantified the three density distributions identically to admittances, see Fig. 3. The correlations are very high, reaching more than 0.99 over the whole spectrum in the nearside and farside highlands. In Mare Crisium, the correlation is smaller between degrees 150-200 and is consistently above 0.975 for $n > 200$. The correlations for the lateral (blue curves) and 3D spatial (red curves) density

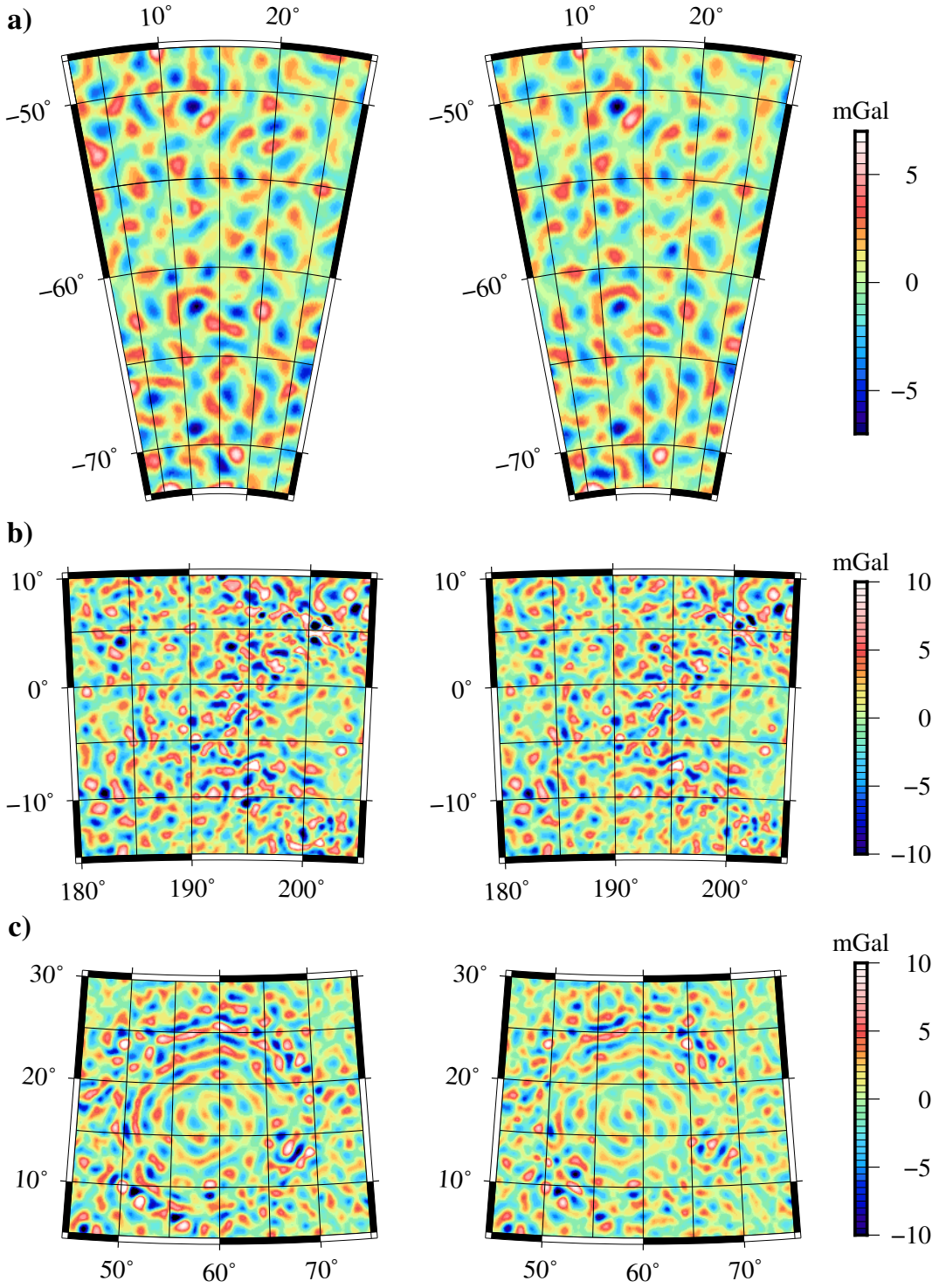

Figure 5: Maps of the Bouguer radial gravitation in: **a)** the nearside highlands, **b)** the farside highlands, and **c)** Mare Crisium. The Bouguer radial gravitations correspond to the crusts of constant (left) and 3D spatially variable (right) density.

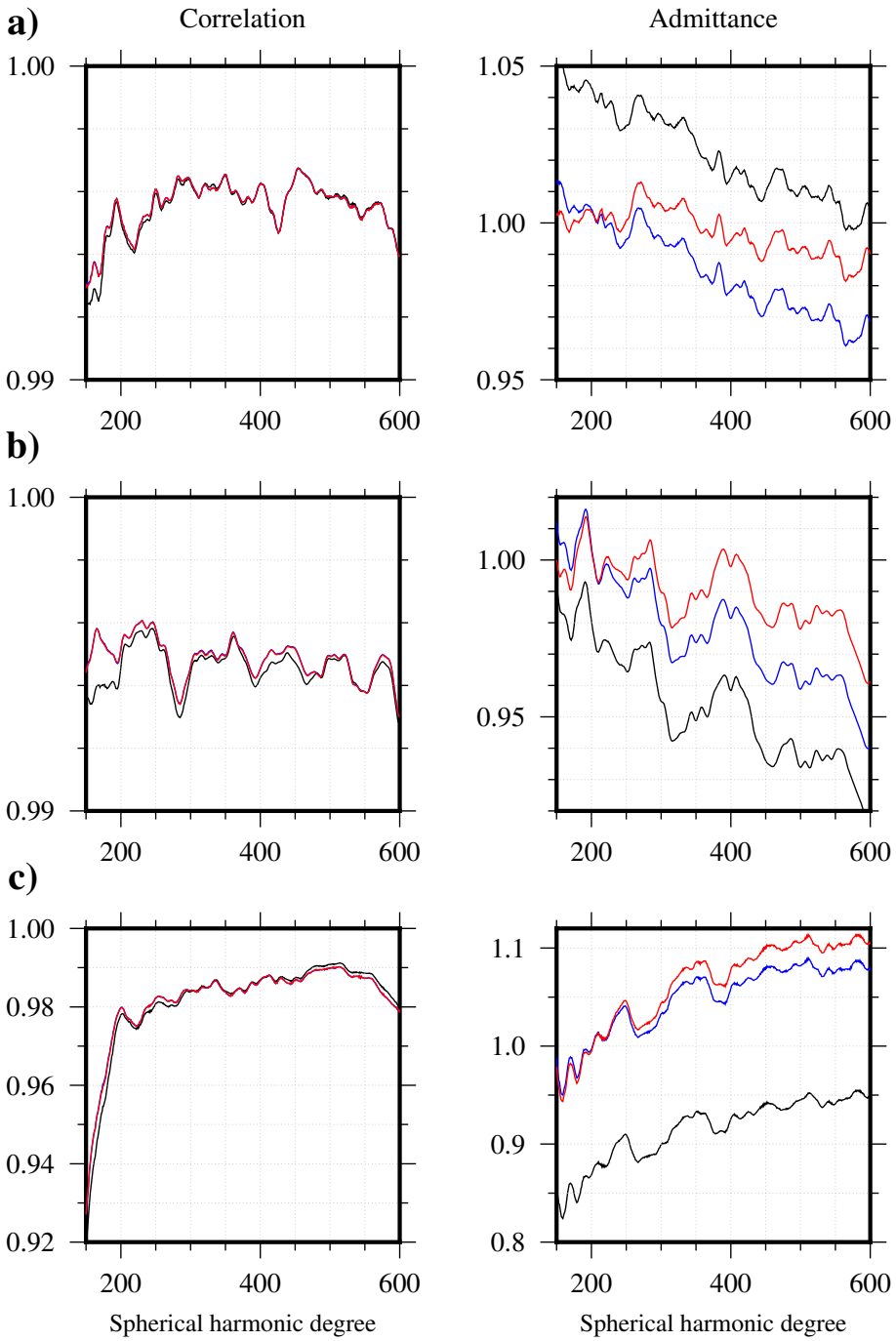

Figure 6: Spectral measures of localised gravitational fields in: **a)** the nearside highlands, **b)** the farside highlands, and **c)** Mare Crisium. The three density distributions are constant (black), laterally variable (blue), and spatially variable (red).

distributions are identical, while those for the uniform density (black curves) are only slightly different.

The admittances discern among the three density distributions. The constant density crust

results in admittances biased from unity. The constant density is underestimated (admittance higher than unity) in the nearside highlands and overestimated (admittance lower than unity) in the farside highlands and in Mare Crisium. On the other, the lateral changes of density provide improved admittance (close to unity) in the three regions. In agreement with the global admittances in Fig. 3, the localised counterparts have the same near-linear trend with increasing harmonic degree for the constant and laterally variable crusts. By considering vertical density variations, our 3D spatially variable crust resulted in most uniform admittance in the nearside and farside highlands. On the other hand, the global linear change of density in the radial direction overestimates the admittance in Mare Crisium in particular for $n > 300$.

3.2. Comparison with GRAIL Level 1B satellite-to-satellite tracking data

Finally, we tested the performance of our three lunar GGFMs beyond degree ∼650 using GRAIL L1B range accelerations taken from `https://pds-geosciences.wustl.edu/grail/grail-l-lgrs-3-cdr-v1/grail_0101/level_1b/`, as the "true" values of line-of-sight gravitation over the high-frequency band such as > 0.1 Hz (e.g., Han, 2013). We used data from the GRAIL Extended Mission from November 30 2012 until December 4 2012 with a temporal sampling of 2 s. Geographically, this dataset covers the central nearside ($\lambda \in [330°, 30°]$) and the central farside ($\lambda \in [150°, 210°]$) of the Moon.

We opted for this time series because the GRAIL satellites orbited at a lower altitude of 20 ± 6.4 km above the LOLA reference sphere of radius 1737.4 km. The gravitational signal of L1B range accelerations at these lower altitudes is sensitive to higher frequency features of the lunar gravitational field. In addition, there were no data gaps during these five consecutive days and no additional pre-processing of the time series, such as interpolation, was required.

For the comparisons, we employed three GRAIL models (GRGM0900C, GRGM1200A, and GL1500E), the two forward models HK2160 and STU2160, and our model implied by the 3D spatially variable density crust. For each model, we synthesised the line-of-sight gravitations along the time series by the formula:

$$\delta\big[\nabla V(r,\varphi,\lambda)\big]\cdot\mathbf{b} = \frac{GM}{R^2}\sum_{n=2}^{\infty}\sum_{m=-n}^{+n}\bar{C}_{n,m}\,\delta\left\{\left(\frac{R}{r}\right)^{n+2}\Big[-b_r\,(n+1)\,\bar{Y}_{n,m}(\varphi,\lambda)\right.$$

$$+ b_\varphi \frac{\partial}{\partial \varphi} \bar{Y}_{n,m}(\varphi, \lambda) - b_\lambda \frac{1}{\cos\varphi} \frac{\partial}{\partial \lambda} \bar{Y}_{n,m}(\varphi, \lambda) \Big] \Bigg\} , \tag{11}$$

where V is the gravitational potential, $\mathbf{b}$ is the unit inter-satellite line-of-sight vector with components $(b_r, b_\varphi, b_\lambda)$, and G is the universal gravitational constant. The symbol δ represents the difference of the same function at two different locations $(r_1, \varphi_1, \lambda_1)$ and $(r_2, \varphi_2, \lambda_2)$ of the two GRAIL satellites. We truncated the infinite series in Eq. (11) at the respective maximum degrees of the six tested models. Eventually, singularities may occur due to the terms $1/\cos\varphi$ and due to the derivative with respect to φ. We implemented the non-singular expressions for the first spatial derivatives of the gravitational potential (e.g., Eshagh, 2008) to avoid this. Moreover, to avoid any numerical problems in computing the associated Legendre functions of the first kind, we incorporated the X-number formulation by Fukushima (2012).

The amplitude spectral densities for the L1B data and for the spherical harmonic GGFMs assessed are depicted in Fig. 7a. The frequency f on the horizontal axis is related to the spherical harmonic degree approximately as $n = 2\pi r f / v$. For the average spherical radius $r = 1757.4$ km and the average velocity $v = 1700$ m s^{-1} of the GRAIL twin-satellites, we obtain a simple relationship $n \approx 6492 f$. Thus, the frequency range $f \in [0.1 \text{ Hz}, 0.25 \text{ Hz}]$ in Fig. 7 corresponds to $n \in [650, 1623]$.

We observe that the amplitude spectral density is considerably lower for STU2160 (magenta curve), due to the coarser topography (shape model) used in its construction (Sect. 1.5) that leads to smoothing of the gravitational spectrum. All other spectra are close to each other up to 0.128 Hz. Above this frequency, the power of GRGM0900C (orange curve) deviates and drops significantly at 0.138 Hz, which corresponds to its maximum harmonic degree of 900. The signal for GRGM1200A (blue curve) weakens at 0.164 Hz and completely loses its power at 0.184 Hz ($n = 1200$). The spectrum of GL1500E (green curve) is similar to that of L1B data up to 0.186 Hz, but starts degrading at 0.204 Hz, and completely drops at 0.23 Hz ($n = 1500$). On the other hand, HK2160 (yellow curve) and our 3D spatially variable crust-inferred model (red curve) do not show any degradation in power out to the Nyquist frequency of 0.25 Hz, because they contain information up to degrees 2160 and 2519, respectively. These two forward models start deviating above 0.216 Hz. Our model possesses higher power than HK2160 in these high frequencies, probably because of the higher resolution topography grid in our analysis. Moreover,

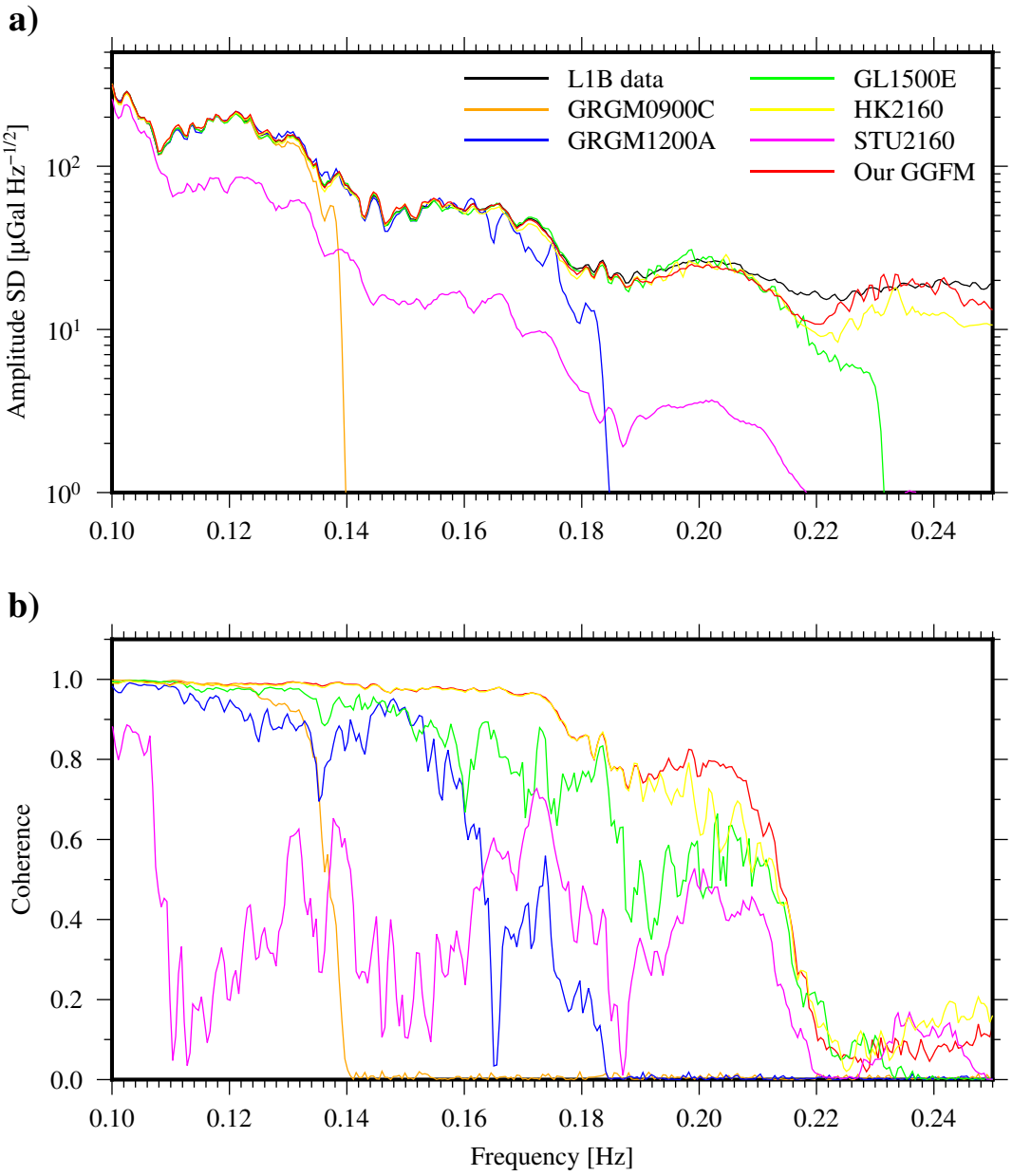

Figure 7: Spectral measures of line-of-sight gravitational accelerations: **a)** the amplitude spectral density and **b)** coherence in the time period from November 30 2012 until December 4 2012.

our model (red curve) provides a better agreement with the raw L1B data (black curve).

Figure 7b illustrates the coherence spectra between the L1B data and the spherical harmonic GGFMs. STU2160's coherence (magenta curve) is seriously degraded and even oscillates. This forward model does not explain the observed gravitational field properly over the depicted frequency range, again most probably due to the use of a coarser topography grid. Among the three GRAIL-only models, GL1500E has a high coherence of 0.8 at 0.184 Hz and 0.5 at 0.21 Hz.

We suspect that GL1500E coherence is higher due to the less stringent power law constraint (constant starting at $n = 700$) and relatively higher weights in the extended mission data, while coherences for GRGM0900C and GRGM1200A are reduced as they employed a more aggressively decreasing power law constraint (starting at $n = 600$). We also note that GRGM1200A performs slightly worse than its predecessor GRGM0900C between the frequencies 0.1 Hz – 0.132 Hz, probably due to different data weighting. The coherences for HK2160 and our model are the highest and almost identical up to 0.19 Hz. However, our model correlates with L1B data better than HK2160 between 0.19 Hz – 0.216 Hz. Coherences for GL1500E, HK2160, and for our crustal model decrease above 0.212 Hz, where L1B data noise overwhelms gravitational signal.

Similar analysis was also performed for the models inferred by the constant and the laterally variable density crustal compositions, but not depicted here. In summary, the corresponding amplitude spectral densities and coherences were almost identical to those from the 3D spatially variable density crust. Thus, the distinctions between our forward model and HK2160 at high-frequencies do not appear to originate from different density assumptions used in these gravitational field models, but are caused most probably by different topographic resolutions. Intuitively, a more detailed topography should be used in forward gravitational field modelling to describe the high-frequency features.

Summary and conclusions

We employed Newton's integral in the spectral domain and solved two geodetic/geophysical tasks for the planetary body of the Moon. Firstly, we formulated a linear, global, and fully spherical mathematical model for crustal density estimation. The observation vector was formed by spherical harmonic coefficients of the gravitational potential, while the components of the design matrix originated from the shape of the topography. We parametrised the laterally variable density part by surface spherical harmonics that allow for various spectral and spatial resolutions. We determined our constant, laterally variable, and 3D spatially variable bulk densities within the lunar crust by using the GL1500E global gravitational field model and LOLA topography. We showed that the constant and laterally variable densities agree with those from previous estimates by other investigators.

Secondly, we used the three distinct crustal compositions for forward calculation of global

gravitational field models up to degree 2519 (equivalent to a spatial resolution of ∼2.2 km at the lunar equator). We showed that the gravitational field implied by the 3D spatially variable density performs the best globally and also represents better agreement with the observed geopotential fields in the nearside and farside highlands. In other regions, however, such as over the lunar maria and low-elevated areas with basaltic lava infills, the gravitational field implied by our 3D spatially variable density should be used with caution, and its simpler counterparts may be preferred.

Finally, we compared six lunar gravitational field models with "independent" Level 1B GRAIL satellite-to-satellite tracking data. The high-frequency signal (a spatial resolution of ∼2 km) of our geopotential model was most consistent with the Level 1B data, while those from GRAIL models weaken, e.g., due to the limited spectral resolution or power law constraints used in their computation.

Our high resolution models with the optimized density variation could be useful for future lunar lander navigation and geophysical exploration.

Acknowledgement: This research was supported financially by the Australian Government through the Australian Research Council's Discovery Projects funding scheme (project DP160104095). Michal Šprlák was also supported by the project LO1506 of the Czech Ministry of Education, Youth and Sports. The global (lateral) density model and the gravitational field models inferred by the three lunar compositions will be publicly available at `https://www.researchgate.net/project/Understanding-the-Moons-crustal-structure-from-analysis-of-new-high-resolution-gravity-topography-and-seismic-data`. GRAIL Level 1B and Level 2 products are publicly available at `https://pds-geosciences.wustl.edu/missions/grail/default.htm`. The forward gravitational field models by Hirt and Kuhn (2017) and Bucha et al. (2019) are publicly available at `http://icgem.gfz-potsdam.de/tom_celestial`.

References

Abramowitz M, Stegun IA (1972) Handbook of mathematical functions with formulas, graphs, and mathematical tables. Tenth Printing, National Bureau of Standards, Department of Commerce, Washington DC, U.S.A., 1046 pp.

Akim EL (1966) Determination of the gravitational field of the Moon from the motion of the artificial lunar satellite Luna-10. Doklady Akademii Nauk SSSR 170:799-802.

Andrews–Hanna JC, Besserer J, Head III JW, Howett CJA, Kiefer WS, Lucey PJ, McGovern PJ, Melosh HJ, Neumann GA, Phillips RJ, Schenk PM, Smith DE, Solomon SC, Zuber MT (2014) Structure and evolution of the lunar Procellarum region as revealed by GRAIL gravity data. Nature 514(7520):68-71. https://doi.org/10.1038/nature13697.

Besserer J, Nimmo F, Wieczorek MA, Weber RC, Kiefer WS, McGovern PJ, Andrews-Hanna JC, Smith DE, Zuber MT (2014) GRAIL gravity constraints on the vertical and lateral density structure of the lunar crust. Geophysical Research Letters 41(16):5771-5777. https://doi.org/10.1002/2014GL060240.

Bouman J (1998) Quality of regularization methods. DEOS Report No. 98.2, Delft University Press, Delft, The Netherlands, 104 pp.

Bucha B, Hirt C, Kuhn M (2019) Divergence-free spherical harmonic gravity field modelling based on the Runge-Krarup theorem: a case study for the Moon. Journal of Geodesy 93(4), 489-513. https://doi.org/10.1007/s00190-018-1177-4.

Eshagh M (2008) Non-singular expressions for vector and gradient tensor of gravitation in a geocentric spherical frame. Computers & Geosciences 34(12):1762-1768. https://doi.org/10.1016/j.cageo.2008.02.022.

Eshagh M (2009) Spherical harmonics expansion of the atmospheric gravitational potential based on exponential and power models of atmosphere. Artificial Satellites 43(1):26-43. https://doi.org/10.2478/v10018-009-0005-8.

Featherstone WE, Hirt C, Kuhn M (2013) Band-limited Bouguer gravity identifies new basins on the Moon. Journal of Geophysical Research – Planets 118(6):1397-1413. https://doi.org/10.1002/jgre.20101.

Fukushima T (2012) Numerical computation of spherical harmonics of arbitrary degree and order by extending exponent of floating point numbers. Journal of Geodesy 86(4):271-285. https://doi.org/10.1007/s00190-011-0519-2.

Garcia F, Gagnepain-Beyneix J, Chevrot S, Lognonné P (2011) Very preliminary reference Moon model. Physics of the Earth and Planetary Interiors 188(1-2):96-113. https://doi.org/10.1016/j.pepi.2011.06.015.

Grafarend EW (2006) Linear and nonlinear models: fixed effects, random effects, and mixed models. Walter de Gruyter, Berlin, Germany, 752 pp.

Han S-C (2013) Determination and localized analysis of intersatellite line of sight gravity difference: Results from the GRAIL primary mission. Journal of Geophysical Research – Planets 118(11):2323-2337. https://doi.org/10.1002/2013JE004402.

Han S-C, Schmerr N, Neumann G, Holmes SA (2014) Global characteristics of porosity and density stratification within the lunar crust from GRAIL gravity and Lunar Orbiter Laser Altimeter topography data. Geophysical Research Letters 41(6):1882-1889. https://doi.org/10.1002/2014GL059378.

Heiskanen WA, Moritz H (1967) Physical geodesy. WH Freeman and Co., San Francisco, U.S.A., 364 pp.

Hirt C, Kuhn M (2017) Convergence and divergence in spherical harmonic series of the gravitational field generated by high-resolution planetary topography - A case study for the Moon. Journal of Geophysical Research – Planets 122(8):1727-1746. https://doi.org/10.1002/2017JE005298.

Jansen JC, Andrews-Hanna JC, Li Y, Lucey PG, Taylor GJ, Goossens S, Lemoine FG, Mazarico E, Head III JW, Milbury C, Kiefer WS, Soderblom JM, Zuber MT (2017) Small-scale density variations in the lunar crust revealed by GRAIL. Icarus 291:107-123. https://doi.org/10.1016/j.icarus.2017.03.017.

Konopliv AS, Asmar SW, Carranza E, Sjogren WL, Yuan D-N (2001) Recent gravity models as a result of the Lunar Prospector mission. Icarus 150:1-18. https://doi.org/10.1006/icar.2000.6573.

Konopliv AS, Park RS, Yuan D-N, Asmar SW, Watkins MM, Williams JG, Fahnestock E, Kruizinga G, Paik M, Strekalov D, Harvey N, Smith DE, Zuber MT (2014) High-resolution

lunar gravity fields from the GRAIL Primary and Extended Missions. Geophysical Research Letters 41(5):1452-1458. https://doi.org/10.1002/2013GL059066.

Laneuville M, Wieczorek MA, Breuer D, Tosi N (2013) Asymmetric thermal evolution of the Moon. Journal of Geophysical Research – Planets 118(7):1435-1452. https://doi.org/10.1002/jgre.20103.

Lemoine FG, Goossens S, Sabaka TJ, Nicholas JB, Mazarico E, Rowlands DD, Loomis BD, Chinn DS, Neumann GA, Smith DE, Zuber MT (2014) GRGM900C: A degree 900 lunar gravity model from GRAIL primary and extended mission data. Geophysical Research Letters 41(10):3382-3389. https://doi.org/10.1002/2014GL060027.

Liang Q, Chen C, Li Y (2014) 3-D inversion of gravity data in spherical coordinates with application to the GRAIL data. Journal of Geophysical Research – Planets 119(6):1359-1373. https://doi.org/10.1002/2014JE004626.

Mazarico E, Neumann GA, Barker MK, Goossens S, Smith DE, Zuber MT (2018) Orbit determination of the Lunar Reconnaissance Orbiter: Status after seven years. Planetary and Space Science 162(1):2-19. https://doi.org/10.1016/j.pss.2017.10.004.

Miller J (2019) Planetary spacecraft navigation. Space Technology Library, Vol. 37, Springer International Publishing, Cham, Switzerland, 390 pp., https://doi.org/10.1007/978-3-319-78916-3.

Melosh HJ, Freed AM, Johnson BC, Blair DM, Andrews–Hanna JC, Neumann GA, Phillips RJ, Smith DE, Solomon SC, Wieczorek MA, Zuber MT (2013) The origin of lunar mascon basins. Science 340(6140):1552-1555. https://doi.org/10.1126/science.1235768.

Moritz H (1989) Advanced physical geodesy, 2nd edition. Wichmann, Karlsruhe, Germany, 500 pp.

Moritz H (1990) The figure of the Earth: theoretical geodesy and the Earth's interior. Wichmann, Karlsruhe, Germany, 279 pp.

Muller PM, Sjogren WL (1968) Mascons: lunar mass concentrations. Science 61(3842):680-684. https://doi.org/10.1126/science.161.3842.680.

Namiki N, Iwata T, Matsumoto K, Hanada H, Noda H, Goossens S, Ogawa M, Kawano N, Asari K, Tsuruta S, Ishihara Y, Liu Q, Kikuchi F, Ishikawa T, Sasaki S, Aoshima C, Kurosawa K, Sugita S, Takano T (2009) Farside gravity field of the Moon from four-way Doppler measurements of SELENE (Kaguya). Science 323(5916):900-905. https://doi.org/10.1126/science.1168029.

Neumann GA, Zuber MT, Wieczorek MA, Head JW, Baker DMH, Solomon SC, Smith DE, Lemoine FG, Mazarico E, Sabaka TJ, Goossens SJ, Melosh HJ, Phillips RJ, Asmar SW, Konopliv AS, Williams JG, Sori MM, Soderblom JM, Miljković K, Andrews–Hanna JC, Nimmo F, Kiefer WS (2015) Lunar impact basins revealed by Gravity Recovery and Interior Laboratory measurements. Science Advances 1(9):e1500852. https://doi.org/10.1126/sciadv.1500852.

Newton I (1687) Philosophiae Naturalis Principia Mathematica.

Novák P, Grafarend EW (2006) The effect of topographical and atmospheric masses on spaceborne gravimetric and gradiometric data. Studia Geophysica et Geodaetica 50(4):549-582. https://doi.org/10.1007/s11200-006-0035-7.

Ramillien G (2002) Gravity/magnetic potential of uneven shell topography. Journal of Geodesy 76(3):139-149. https://doi.org/10.1007/s00190-002-0193-5.

Sjogren WL, Wimberly RN, Wollenhaupt WR (1974) Lunar gravity via the Apollo 15 and 16 subsatellites. Moon 9(1-2):115-128. https://doi.org/10.1007/BF00565398.

Smith DE, Zuber MT, Neumann GA, Lemoine FG, Mazarico E, Torrence MH, McGarry JF, Rowlands DD, Head III JW, Duxbury TH, Aharonson O, Lucey PG, Robinson MS, Barnouin OS, Cavanaugh JF, Sun X, Liiva P, Mao D-D, Smith JC, Bartels AE (2010) Initial observations from the Lunar Orbiter Laser Altimeter (LOLA). Geophysical Research Letters 37(18):L18204. https://doi.org/10.1029/2010GL043751.

Šprlák M, Han S-C, Featherstone W (2018) Forward modelling of global gravity fields with 3D density structures and an application to the high-resolution (∼2 km) gravity fields of the Moon. Journal of Geodesy 92(8):847-862. https://doi.org/10.1007/s00190-017-1098-7.

Wahl D, Oberst J (2019) Lateral variations in bulk density and porosity of the upper lunar crust from high-resolution gravity and topography data: comparison of different analysis techniques. ISPRS Annals of the Photogrammetry, Remote Sensing and Spatial Information Sciences IV-2/W5:527-532. https://doi.org/10.5194/isprs-annals-IV-2-W5-527-2019.

Wessel P, Smith WHF, Scharroo R, Luis JF, Wobbe F (2013) Generic Mapping Tools: Improved version released. EOS – Transactions of the AGU 94(45):409-410. https://doi.org/10.1002/2013EO450001.

Wieczorek MA, Neumann GA, Nimmo F, Kiefer WS, Taylor GJ, Melosh HJ, Phillips RJ, Solomon SC, Andrews-Hanna JC, Asmar SW, Konopliv AS, Lemoine FG, Smith DE, Watkins MM, Williams JG, Zuber MT (2013) The crust of the Moon as seen by GRAIL. Science 339(6120):671-675. https://doi.org/10.1126/science.1231530.

Wieczorek MA, Phillips RJ (1998) Potential anomalies on a sphere: applications to the thickness of the lunar crust. Journal of Geophysical Research –Planets 103(E1):1715-1724. https://doi.org/10.1029/97JE03136.

Wieczorek MA, Simons FJ (2005) Localized spectral analysis on the sphere. Geophysical Journal International 162(3):655-675. https://doi.org/10.1111/j.1365-246X.2005.02687.x.

Williams JG, Konopliv AS, Boggs DH, Park RS, Yuan D-N, Lemoine FG, Goossens S, Mazarico E, Nimmo F, Weber RC, Asmar SW, Melosh HJ, Neumann GA, Phillips RJ, Smith DE, Solomon SC, Watkins MM, Wieczorek MA, Andrews–Hanna JC, Head JW, Kiefer WS, Matsuyama I, McGovern PJ, Taylor GJ, Zuber MT (2014) Lunar interior properties from the GRAIL mission. Journal of Geophysical Research – Planets 119(7):1546-1578. https://doi.org/10.1002/2013JE004559.

Zhang Y, Wu Y, Yan J, Wang H, Rodriguez JAP, Qiu Y (2018) 3D inversion of full gravity gradient tensor data in spherical coordinate system using local north-oriented frame. Earth, Planets and Space 70(1):58. https://doi.org/10.1186/s40623-018-0825-5.

Zhao G, Chen B, Uieda L, Liu J, Kaban MK, Chen L, Guo R (2019) Efficient 3-D large-scale forward modeling and inversion of gravitational fields in spherical coordinates with appli-

cation to lunar mascons. Journal of Geophysical Research – Solid Earth 124(4):4157-4173. https://doi.org/10.1029/2019JB017691.

Zhong Z, Yan J, Jin S, Zhu M, Rodriguez JAP, Zhu H, Li Y (2019) Selenophysical parameter inversion in the Lunar Southern Hemisphere Highland based on mutant particle swarm optimization. Physics of the Earth and Planetary Interiors 292:55-66. https://doi.org/10.1016/j.pepi.2019.05.001.

Zuber MT, Smith DE, Lemoine FG, Neumann GA (1994) The shape and internal structure of the Moon from the Clementine mission. Science 266(5192):1839-1843. https://doi.org/10.1126/science.266.5192.1839.

Zuber MT, Smith DE, Lehman DH, Hoffman TL, Asmar SW, Watkins MM (2013) Gravity Recovery and Interior Laboratory (GRAIL): mapping the lunar interior from crust to core. Space Science Reviews 178(1):3-24. https://doi.org/10.1007/s11214-012-9952-7.